

Transient Laser-Induced Breakdown of Dielectrics in Ultrarelativistic Laser-Solid Interactions

Constantin Bernert^{1,2,*}, Stefan Assenbaum^{1,2}, Stefan Bock¹, Florian-Emanuel Brack¹, Thomas E. Cowan^{1,2}, Chandra B. Curry^{3,4}, Marco Garten^{1,†}, Lennart Gaus^{1,2}, Maxence Gauthier^{1,3}, René Gebhardt¹, Sebastian Göde⁵, Siegfried H. Glenzer^{1,3}, Uwe Helbig¹, Thomas Kluge¹, Stephan Kraft¹, Florian Kroll¹, Lieselotte Obst-Huebl^{1,†}, Thomas Püschel¹, Martin Rehwald¹, Hans-Peter Schlensvoigt¹, Christopher Schoenwaelder^{1,3,6}, Ulrich Schramm^{1,2}, Franziska Treffert^{1,7}, Milenko Vescovi¹, Tim Ziegler^{1,2}, and Karl Zeil¹

¹Helmholtz-Zentrum Dresden—Rossendorf, Dresden 01328, Germany

²Technische Universität Dresden, Dresden 01062, Germany

³SLAC National Accelerator Laboratory, Menlo Park, California 94025, USA

⁴University of Alberta, Edmonton, Alberta T6G 1H9, Canada

⁵European XFEL GmbH, Schenefeld 22869, Germany

⁶Friedrich-Alexander Universität Erlangen-Nürnberg, Erlangen 91054, Germany

⁷Technische Universität Darmstadt, Darmstadt 64289, Germany



(Received 28 July 2022; revised 2 December 2022; accepted 16 December 2022; published 30 January 2023)

For high-intensity laser-solid interactions, the absolute density and surface density gradients of the target at the arrival of the ultrarelativistic laser peak are critical parameters. Accurate modeling of the leading edge-driven target preexpansion is desired to strengthen the predictive power of associated computer simulations. The transition from an initial solid state to a plasma state, i.e., the breakdown of the solid, defines the starting point of the subsequent target preexpansion. In this work, we report on the time-resolved observation of transient laser-induced breakdown (LIB) during the leading edge of high-intensity petawatt-class laser pulses with peak intensities of up to $5.7 \times 10^{21} \text{ W/cm}^2$ in interaction with dielectric cryogenic hydrogen jet targets. LIB occurs much earlier than what is typically expected following the concept of barrier suppression ionization. The observation is explained by comparing a characterization study of target-specific LIB thresholds with laser contrast measurements. The results demonstrate the relevance of the laser pulse duration dependence of LIB for high-intensity laser-solid interactions. We provide an effective approach to determine the onset of LIB and thereby the starting point of target preexpansion in other laser-target systems.

DOI: 10.1103/PhysRevApplied.19.014070

I. INTRODUCTION

High-intensity laser-solid interactions are used in a variety of applications such as fast ignition for inertial confinement fusion [1,2], plasma-based particle accelerators [3], warm dense matter research [4–7], time-resolved studies of transient fields [8,9], and translational research for radiation oncology [10,11]. Control over the amount of

light that precedes the high-intensity laser pulse (temporal “leading edge”) is of particular importance, e.g., for reaching high particle energies in laser-ion acceleration [12–14]. Great progress has been made to improve the contrast ratio between the pulse leading edge and the peak intensity (“laser contrast”) of available terawatt and petawatt systems [15] by dedicated adaptation of the laser technology [16], second-harmonic generation of the compressed high-power laser beam [17] and the implementation of plasma mirrors [18,19], accompanied by the development of specialized optical measurement devices [20–24]. Still, quantitative agreement between the results of experiments and simulations of high-intensity laser-solid interactions is rare. The consistent simulation of all parts of the interaction, starting with the solid-state structure of the initially cold target, through the ionization process with the phase transition to the plasma state and the regimes of collisional

* c.bernert@hzdr.de

† Present address: Lawrence Berkeley National Laboratory, Berkeley, California, 94720, USA.

Published by the American Physical Society under the terms of the [Creative Commons Attribution 4.0 International license](#). Further distribution of this work must maintain attribution to the author(s) and the published article’s title, journal citation, and DOI.

and resonance laser absorption, to the collisionless relativistic regime, i.e., a complete “start-to-end simulation,” is challenging in several aspects. At low laser intensity, the interaction is governed by the energy scales of the solid-state lattice, while at high intensity the laser fields start to dominate and particle motion becomes highly kinetic. For intermediate intensities, collective electronic motion mediates the energy transfer to the highly collisional particle system. Today, target preexpansion by the leading edge is usually treated only in a simplified way, for example by adding a plasma scale length on the target front and rear side as a starting condition of a particle-in-cell (PIC) simulation of the relativistic laser-target interaction. More ambitious approaches, such as the sequence of a radiation-hydrodynamics simulation for the subrelativistic intensities in the leading edge followed by a PIC simulation for the relativistic intensities around the laser peak [25–27], are rare but essential for predictive numerical modeling [28]. Interestingly, the highest-energy laser-accelerated proton beams were measured from targets made of cryogenic hydrogen or plastic foils [29–32], all of which are dielectric targets. Start-to-end simulations of petawatt-class lasers in interaction with dielectric solids are therefore of particular interest.

The starting point of the numerical treatment, which means the classification into relevant and negligible laser intensities, is essential for start-to-end simulations. With the removal of the lattice bonds, the laser-induced breakdown of the solid constitutes a reasonable onset for a plasma-hydrodynamics modeling of the target preexpansion by the leading edge. Commonly, this starting point is estimated using the measured laser contrast and a threshold intensity like the *appearance intensity* I_{app} [33]. The appearance intensity I_{app} corresponds to the critical field of *barrier suppression ionization* (BSI threshold) [34]. At this intensity, the ionization potential of the outermost bound electron of the target atoms is balanced by the electric field strength of the laser. A classical treatment gives

$$I_{\text{app}}(\text{W/cm}^2) \approx 4 \times 10^9 \times E_{\text{ip}}(\text{eV})^4 / Z_{\text{eff}}^2 \quad (1)$$

with Z_{eff} being the charge state of the atom after ionization and E_{ip} the ionization potential of the $Z_{\text{eff}} - 1$ charge state, e.g., tabulated in Ref. [35]. A quantum mechanical treatment yields somewhat higher values of the critical field [36].

The laser-induced breakdown of solids is an extensively studied field and the occurrence of different melting mechanisms leads to a significant variation of the laser-induced damage threshold (LIDT) intensity well below the BSI threshold for varied laser parameters [37]. For metallic solids, the laser energy is directly absorbed by quasifree electrons in the conduction band and it is subsequently transferred to the lattice by collisions. It follows that, for a broad range of laser parameters, the phase transition

of metals is very similar to classical melting. Dielectric solids, however, are transparent to the incident laser light and a single photon is insufficient to bridge the band gap. They generally exhibit higher LIDT intensities than metals. LIDT measurements with femtosecond and picosecond laser pulses show a significant variation of the threshold with laser pulse duration, target material, and thickness [38–40]. Furthermore, not only the laser fluence but also the specific temporal envelope of the intensity is relevant [41–44].

The variation of thresholds results from an interplay of different ionization mechanisms in different intensity and pulse duration regimes. Barrier suppression ionization occurs at intensities above the BSI threshold [36]. Below it and depending on the laser pulse duration, the two driving mechanisms are *strong field ionization*, i.e., tunnel and multiphoton ionization (see Keldysh theory [45,46]), and *avalanche ionization* (also called *impact ionization*) [37–39]. Avalanche ionization is based on continuous laser heating of conduction-band electrons that subsequently ionize valence-band electrons by collisions. By accumulation of laser energy on target, the number of conduction-band electrons increases nonlinearly (avalanche effect), with recombination counteracting. In fused silica, which is a dielectric solid with a large band gap of about 9 eV, all three ionization mechanisms are relevant for a quantitative agreement of simulations to single-shot LIDT data, with avalanche ionization becoming predominant at pulse durations $\gtrsim 50$ fs [47,48]. Simulations of macroscopic ionization dynamics are usually based on single-, multiple-, or dynamic rate equations [47–51] and nowadays provide quantitative agreement with experimental LIDT results over a wide range of laser pulse durations.

Because of technical limitations in the amplification chain [15] of a petawatt-class laser system (e.g., Refs. [52–55]), the leading edge of an amplified pulse typically exhibits distinct short-pulse prepulses, a subjacent continuous pedestal of varying slope, and a steep rising edge towards the laser peak. To avoid target preexpansion, the individual segments of a given leading edge can be compared to target-specific LIDT values. Because LIDT intensity varies with laser pulse duration, different parts of the leading edge are expected to trigger breakdown by exceeding different thresholds [40]. Still, the occurrence of the effect in an actual high-intensity laser-solid interaction has yet to be demonstrated.

LIDT values are commonly measured from target fracture, e.g., hole diameter, and represent time-integrated measurements. For high-intensity laser-solid interactions, however, the breakdown is a transient effect and accounts for only a specific part of the overall interaction. In a start-to-end simulation of a high-intensity laser interaction with a dielectric target, the transient formation of a quasifree electron density above the critical plasma density and the abruptly occurring change of the optical properties [56]

is the relevant parameter. In the following, we call this transient formation “transient laser-induced breakdown” (LIB). LIB can be considered as part of the temporal evolution towards LIDT. In fact, exceeding the critical plasma density is one of the ways to define LIDT in rate equation models for simulating dielectric breakdown [39].

In this work, we experimentally show the impact of the pulse duration dependence of LIB on the onset of LIB in high-intensity laser-solid interactions and present a method of how the observations can be utilized for other laser-target systems.

For demonstration, we use the interaction between petawatt-class high-contrast laser pulses with peak intensities from 0.6×10^{21} to $5.7 \times 10^{21} \text{ W/cm}^2$ and a dielectric cryogenic hydrogen jet target [57,58]. As hydrogen has only one bound electron per atom, it is a particularly basic example for the investigation of ionization effects. In addition, because the micrometer-sized jet target is easily accessible and can be diagnosed from different angles, it is an excellent target test bed to study specific issues of high-intensity laser-solid interactions in combination with optical probing diagnostics [59–63]. In particular, time-resolved off-harmonic optical shadowgraphy [63] is ideally suited to inspect the occurrence of LIB, because it overcomes the issue of plasma self-emission and reveals target areas where LIB occurs as blackened regions within the otherwise transparent target.

The paper is structured as follows. In Sec. II, we present the experimental setup and a characterization study of the target-specific LIB thresholds for different laser pulse durations. In Sec. III, experimental measurements of LIB within the leading edge of an ultrarelativistic laser pulse interacting with a hydrogen jet target are reported and related to a measurement of the temporal laser contrast in Sec. IV. After an outlook on future experiments in Sec. V, Sec. VI concludes our work.

II. EXPERIMENTAL SETTINGS

A. Setup

The experiment is conducted with the DRACO petawatt laser [64] at the Helmholtz-Zentrum Dresden-Rossendorf (HZDR) and the experimental setup is shown in Fig. 1(a). The DRACO laser (hereafter called “pump laser,” 800 nm central wavelength, 30 fs pulse duration, 19 J pulse energy, *p*-polarized) is focused via an *f*/2.5 off-axis parabola (OAP) to a spot size of $2.6 \mu\text{m}$ full width at half maximum (FWHM). This results in a peak intensity of $5.7 \times 10^{21} \text{ W/cm}^2$, which can be tuned between 10% and 100% by changing the amplification of the final laser amplifier. A recollimating single plasma mirror setup is utilized to achieve high temporal contrast ($>10^{-8}$ at -2 ps , $>10^{-10}$ at -10 ps , singular short prepulse with 10^{-9} at -54 ps ; see Appendix B). A continuously flowing sheet jet of solid

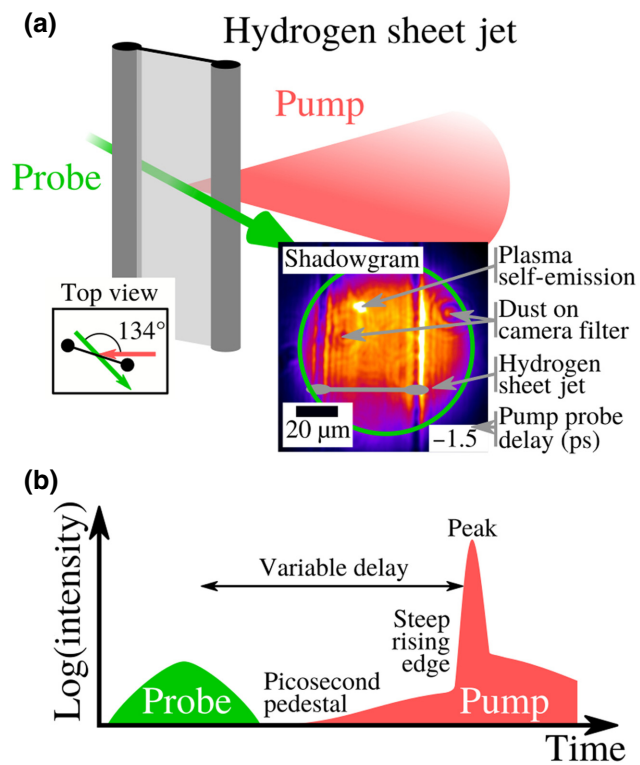


FIG. 1. (a) Experimental setup (not to scale): high-intensity pump laser is focused onto the hydrogen sheet-jet target. Optical probe pulses enable time-resolved shadowgraphy. (b) Temporal schematic of the setup, with the probe laser pulse preceding the pump laser pulse. The specific characteristics of the leading edge of the high-intensity pump laser are explicitly labeled.

hydrogen [57,58] with $60 \mu\text{m}$ width serves as a dielectric target with a total electron density of $n_e^{\text{jet}} = 5.2 \times 10^{22} \text{ cm}^{-3}$, hcp and fcc crystal structure [65], and a band gap of about 10.9 eV [66]. As sketched in Fig. 1(a), the planar sheetlike part with a thickness of approximately 400 nm is formed between two prominent cylindrical rims. The experiment is conducted at target rotation angles between 65° and 80° (target normal to pump laser).

Time-resolved optical shadowgraphy data of the pump laser-target interaction are recorded by off-harmonic optical probing using a 515-nm, 160-fs backscatterer at 134° relative to the pump laser axis [see the top view inset in Fig. 1(a)]. The spatial resolution limit of the imaging system is $1.5 \mu\text{m}$ and the temporal resolution of time delays is 175 fs. A pump-probe delay of 0 ps corresponds to the arrival of the pump laser peak on target and negative delays represent earlier times. The setup was utilized in previous experiments and details are available in Ref. [63]. The observable general structures in the recorded shadowgraphy images are illustrated in the inset of Fig. 1(a). A secondary optical probing axis at 69° guarantees control over the target rotation angle for each shot (not shown here for simplicity).

Figure 1(b) shows the typical temporal properties of the leading edge of the pump laser. The *peak* is preceded by a *steep rising edge* and a more shallow *picosecond pedestal*. The temporal resolution of a delay scan via shadowgraphy allows the pump laser-target interaction to be scanned especially within the picosecond pedestal region.

B. Pulse duration dependence of LIB

The individual segments of the leading edge of the pump laser can be characterized by their temporal slope. For high-intensity lasers with a pulse duration of a few tens of femtoseconds, such as the DRACO laser, the intensity within the steep rising edge typically increases by an order of magnitude in less than 100 fs. The intensity in the picosecond pedestal, however, increases more slowly, by an order of magnitude in single to tens of picoseconds. To identify the relevant order of magnitude in intensity for LIB, we perform a characterization study using reduced laser peak intensity and laser pulse durations from 29 fs to 6.3 ps (details in Appendix A). Although none of the temporal envelopes of the utilized pulses exactly match individual segments of the leading edge, pulses with tens to hundreds of femtoseconds duration can approximate the steep rising edge or singular short prepulses. Pulses of multiple picoseconds duration with a more super-Gaussian envelope can approximate the slowly rising picosecond pedestal.

As the main result of the characterization study, the intensity and fluence threshold values of LIB, I_{th} and F_{th} , are presented in Fig. 2. For each pulse duration, I_{th} and F_{th} mark the thresholds at which a transiently blackened target area, i.e., an area undergoing LIB, is observed by using time-resolved optical shadowgraphy (details in Appendix A). Thus, the measured thresholds compare particularly well with the time-resolved measurements at ultrarelativistic peak intensity in the next section. The thresholds show a high dependence on the FWHM laser pulse duration τ . Power-law fits to the thresholds of intensity I_{th} and fluence F_{th} (orange lines) yield the scalings

$$I_{\text{th}}^{\text{fit}}(\text{W/cm}^2) = 8.3 \pm 0.5 \times 10^{12} \times \tau(\text{ps})^{-0.71 \pm 0.03} \quad (2)$$

and

$$F_{\text{th}}^{\text{fit}}(\text{J/cm}^2) = 8.0 \pm 0.4 \times \tau(\text{ps})^{0.24 \pm 0.02}. \quad (3)$$

To estimate the contribution of the different underlying ionization mechanisms, the results are compared below with the literature on LIDT of fused silica (FS), which has a band gap (about 9 eV) that almost reaches that of solid hydrogen (about 10.9 eV). Recently, a dynamical rate equation model was used to investigate the contribution of avalanche ionization and strong field ionization to the scaling of the damage fluence of fused silica $F_{\text{th}}^{\text{FS}}[\tau]$ for pulse durations between 10 fs and 4 ps in Ref. [48]. They

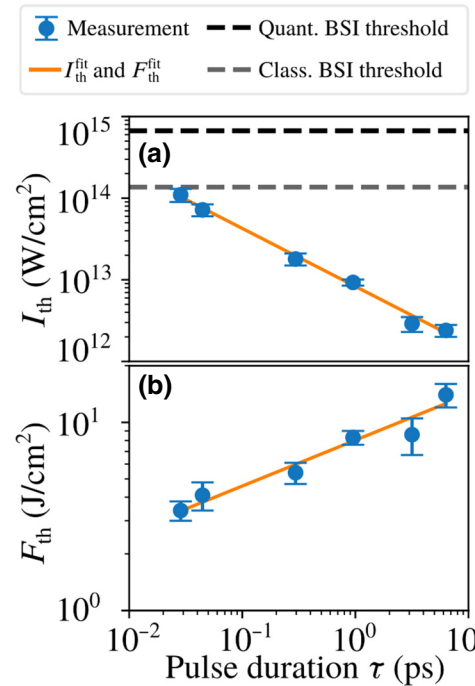


FIG. 2. (a) Measured intensity thresholds I_{th} and (b) fluence thresholds F_{th} of LIB of the hydrogen sheet-jet target versus FWHM laser pulse duration τ (blue dots). The pump laser settings of each measurement are given in Table II in Appendix A. Power-law fits to the data yield $I_{\text{th}}^{\text{fit}} \propto \tau^{-0.71 \pm 0.03}$ [orange line in (a), Eq. (2)] and $F_{\text{th}}^{\text{fit}} \propto \tau^{0.24 \pm 0.02}$ [orange line in (b), Eq. (3)]. The quantum mechanical BSI threshold (black) and the classical BSI threshold (gray) are given by dashed horizontal lines in (a).

showed that strong field ionization alone yields a too strong pulse duration scaling of LIDT and that the inclusion of avalanche ionization is required to support a scaling that fits the experimental data. Even for pulse durations down to tens of femtoseconds, the inclusion of avalanche ionization in the rate equation model is necessary to explain the experimental data quantitatively. The findings are supported by earlier work at pulse durations between 7 and 300 fs, where it is concluded that avalanche ionization is predominant at pulse durations >50 fs and increases in relevance with pulse duration [47]. The pulse duration scaling of fused silica $F_{\text{th}}^{\text{FS}} \propto \tau^{0.3}$ [48] is similarly weak as the scaling we find for LIB of solid hydrogen $F_{\text{th}}^{\text{fit}} \propto \tau^{0.24}$.

TABLE I. Measured onset intervals of LIB versus pump laser peak intensity as adopted from Fig. 3. The pump laser pulse duration is 30 fs FWHM.

Peak intensity (W/cm^2)	Onset interval (ps)
0.6×10^{21}	$[-0.6, -0.4]$
1.1×10^{21}	$[-2.0, -1.2]$
2.2×10^{21}	$[-3.1, -2.5]$
5.7×10^{21}	$[-3.9, -2.7]$

From this and taking into account the comparable band gap we assume that LIB of solid hydrogen in the presented pulse duration regime is also due to significant contributions of avalanche ionization, similar to fused silica. More quantitative conclusions would require detailed numerical modeling.

For the laser parameters used in this study, the BSI threshold can serve as an upper estimate of possible threshold intensities of LIB. The appearance intensity of atomic hydrogen $I_{\text{app}}^{\text{H}} = 1.37 \times 10^{14} \text{ W/cm}^2$ (“classical BSI threshold”) is shown as a gray dashed line in Fig. 2(a). However, a nonsimplified quantum mechanical treatment of the hydrogen atom yields a higher critical field of barrier suppression ionization and a corresponding appearance intensity of $7.58 \times 10^{14} \text{ W/cm}^2$ [“quantum mechanical BSI threshold,” black dashed line in Fig. 2(a)] [36].

III. RESULTS

A. Shadowgraphy at ultrarelativistic laser peak intensity

The experiments in the ultrarelativistic regime with peak intensities between 0.6×10^{21} and $5.7 \times 10^{21} \text{ W/cm}^2$ are conducted with the nominal pump laser settings at 30 fs FWHM pulse duration, as described in Sec. II A. Time delay scans of the shadowgraphy diagnostic at four different peak intensities are shown in Fig. 3. For all peak intensity settings, shadowgrams without and with blackened target areas, i.e., areas where the target experiences dielectric breakdown, are captured. The pump-probe delay intervals within which LIB occurs (“onset interval of LIB”) are given in Table I. The upper boundary of the interval is given by the delay of the earliest shadowgram with an area of dielectric breakdown and the lower boundary is given by the closest delay of a shadowgram without such observation. Note that the width of the onset interval is mainly limited by the available number of shadowgrams and their respective pump-probe delay. As illustrated by the green line and gray shaded background in Fig. 3, we observe a clear shift of the onset interval of LIB to an earlier pump-probe delay with increasing peak intensity.

Depending on the intensity setting and the pump-probe delay, the areas with dielectric breakdown have different contours and patterns. Generally, with increasing delay, the spatial extent of the area grows until it fills the whole field of view ($\text{FOV} = 100 \times 100 \mu\text{m}^2$) close to zero delay. Up to a delay of about -0.4 ps, the areas with dielectric breakdown show sharp contours with larger width than height, exemplified by the shadowgram labeled “ α .” For this and similar shadowgrams, the contour represents the spatial distribution of light with intensities exceeding the threshold of LIB during the leading edge [67]. The aspect ratio of width and height of the area corresponds to the projected shape of the focal spot on the rotated target at a time given by the pump-probe delay.

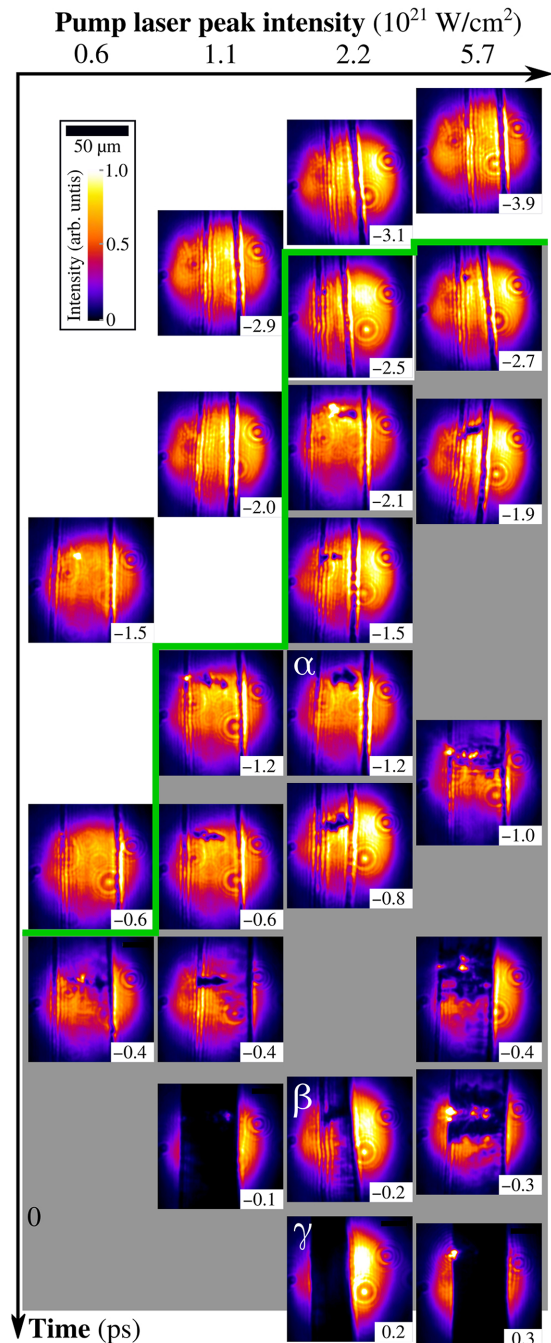


FIG. 3. Shadowgraphy images at different pump laser peak intensities and pump-probe delays (in picoseconds, bottom of each image). Shadowgrams without dielectric breakdown (white background) are separated from shadowgrams with dielectric breakdown (gray background) by the green line.

For pump-probe delays between -0.4 ps and zero, an additional large-scale contour with spatially varying opacity is observed (e.g., the shadowgram labeled “ β ”). The additional contour is most likely caused by relativistic electrons that are generated when the pump laser intensity surpasses about 10^{18} W/cm^2 [68]. For the peak intensities

and laser contrast settings discussed here, this occurs a few hundred femtoseconds before the pump laser peak reaches the target [32]. The laser-heated relativistic electrons traverse the target in all directions, induce return currents, and are known to cause collisional ionization and field ionization on a large spatial scale even for much lower pump laser peak intensities [69]. The spatially varying opacity is caused by differences in the local conduction-band electron density close to the critical plasma density of the probe wavelength $n_c^{515\text{nm}} = 4.2 \times 10^{21} \text{ cm}^{-3}$ [56]. In contrast, shadowgrams captured very close to or later than zero delay show a high opacity within the whole FOV, an area with a diameter about 40 times larger than the FWHM of the focal spot (e.g., the shadowgram labeled “ γ ”). In the corresponding areas, the amount of quasifree electrons equals or is above $n_c^{515\text{nm}}$, i.e., the target experienced dielectric breakdown and the ionization degree of the target is above about 8% = $n_c^{515\text{nm}}/n_e^{\text{jet}}$. For the highest as well as for the lowest peak intensity settings, a secondary shadowgraphy axis with a 1030-nm short-pulse backscatter shows the high opacity within an area greater than 390 μm (limited by the FOV). The ionization degree of the target within this area is above 2% accordingly.

B. Comparison to the laser contrast measurement

The comparison of the measured onset intervals of LIB (Table I) to a laser contrast measurement of the pump laser leading edge is presented in Fig. 4. The laser contrasts of the highest ($5.7 \times 10^{21} \text{ W/cm}^2$) and the lowest ($0.6 \times 10^{21} \text{ W/cm}^2$) peak intensity settings are given in red and blue, respectively. The laser contrast is measured with a third-order autocorrelator and it is scaled to the respective peak intensity on target (for details, see Appendix B). The steep rising edge is visible between -0.4 ps and zero, while the actual temporal shape is smeared out by the temporal resolution of the measurement (about 100 fs). The more slowly rising picosecond pedestal is shown between -12 ps and about -1 ps. The relative intensities of the measurement are commonly used to compare different high-power laser systems [15].

For the highest peak intensity setting, the measured onset interval of LIB (red shaded) lies within the picosecond pedestal. Between about -10 ps and about -3 ps the picosecond pedestal includes a plateau with intensities fluctuating from about 10^{11} W/cm^2 to about 10^{12} W/cm^2 . The onset interval of LIB is located at the end of the plateau and no standout signature of intensity is observed during the interval. In particular, the prepulse at about -2.3 ps is well separated from the observation of LIB at -2.7 ps. For the lowest peak intensity setting, the measured onset interval of LIB (blue shaded) is located within the foot of the steep rising edge.

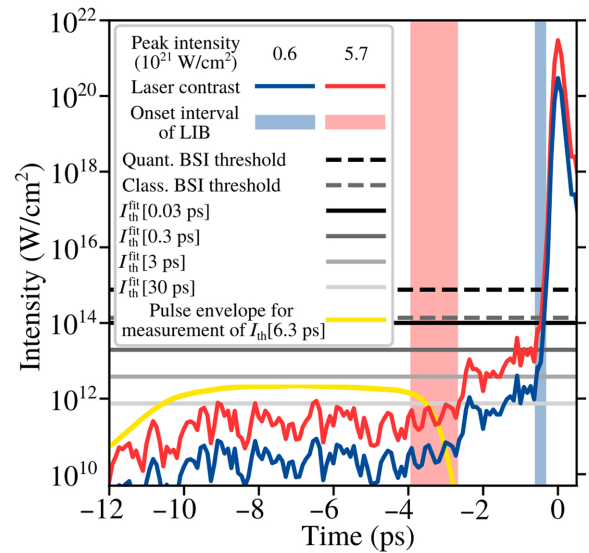


FIG. 4. Laser contrast measurement of the leading edge normalized to the highest (red) and the lowest (blue) peak intensities on target versus the respective onset interval of LIB. The quantum mechanical and classical BSI thresholds are given together with the fitted intensity thresholds of LIB $I_{\text{th}}^{\text{fit}}[\tau]$ for four different pulse durations τ (horizontal lines). The yellow line gives the temporal envelope of the laser pulse utilized for the measurement of $I_{\text{th}}[6.3 \text{ ps}]$. The temporal position is chosen for comparability with the laser contrast in the highest peak intensity setting.

To discuss both settings along with the results of the characterization study on LIB (Fig. 2), the quantum mechanical and classical BSI threshold intensities together with values of $I_{\text{th}}^{\text{fit}}[\tau]$ for different pulse durations τ between 0.03 and 30 ps are given as horizontal lines of different style.

IV. DISCUSSION

In the lowest peak intensity setting, the intersection points of the laser contrast with the quantum mechanical BSI threshold, the classical BSI threshold, the threshold intensity $I_{\text{th}}^{\text{fit}}[0.03 \text{ ps}]$, and $I_{\text{th}}^{\text{fit}}[0.3 \text{ ps}]$ are all located close to each other between -0.32 ps (quantum mechanical BSI threshold) and -0.43 ps ($I_{\text{th}}^{\text{fit}}[0.3 \text{ ps}]$). Within the errorbars, this whole cluster of intersection points is in agreement with the experimental observation and the intensities of the laser contrast suggest a minimum applicable threshold intensity of $4 \times 10^{12} \text{ W/cm}^2 = I_{\text{th}}^{\text{fit}}[2.8 \text{ ps}]$. The agreement between the shadowgraphy measurement and the intersection point of the laser contrast with the classical BSI threshold demonstrates that the appearance intensity I_{app} can be a convenient estimate to determine the starting point of LIB in interactions with similar target properties and similar or lower intensities in the pump laser leading edge.

This changes as the peak intensity is increased by a factor of 10 to $5.7 \times 10^{21} \text{ W/cm}^2$. For the corresponding

leading edge, the intersection of the laser contrast with the classical BSI threshold at -0.44 ps overestimates the starting point of LIB substantially. The same applies to the intersection with threshold intensities $I_{\text{th}}^{\text{fit}}[0.3 \text{ ps}]$ at -1.14 ps and $I_{\text{th}}^{\text{fit}}[3 \text{ ps}]$ at -2.48 ps. This reveals that, for this setting, the simple BSI threshold cannot be used as a criterion for estimating the starting point of LIB based on the laser contrast measurement. Instead, the setting demonstrates that LIB is reached by accumulation of intensity on target and not by crossing a certain intensity level. In the plateau of the picosecond pedestal between -10 and -3 ps, the intensities are close to the thresholds of LIB for picosecond pulses. Comparing -10 and -3 ps, there is no significant difference in the intensity level, except for the amount of temporally “accumulated intensity,” which corresponds to the fluence. As argued in Sec. II B, the contribution of avalanche ionization to LIB of the target used here is relevant and most likely increases with pulse duration. It follows that the described scenario is probably an illustrative example where avalanche ionization during the picosecond pedestal of the leading edge contributes to LIB.

To quantitatively compare the results at $5.7 \times 10^{21} \text{ W/cm}^2$ peak intensity with the characterization study of LIB, the temporal pulse envelope of a 6.3-ps pulse as used in the characterization study is plotted by a yellow line in Fig. 4. For illustration purposes, the pulse is placed before the measured onset of LIB. The peak intensity of the pulse is scaled to $I_{\text{th}}[6.3 \text{ ps}] = (2.4 \pm 0.4) \times 10^{12} \text{ W/cm}^2$, ensuring that a similar pulse induces LIB of the target *after* interaction. The area under the curve corresponds to the threshold fluence $F_{\text{th}}[6.3 \text{ ps}] = (14 \pm 2) \text{ J/cm}^2$. An integration of the laser contrast measurement between -12 and -3 ps yields a fluence of 2.2 J/cm^2 with a highest intensity of $9 \times 10^{11} \text{ W/cm}^2$. It follows that the fluence of the laser contrast measurement is a factor of 6 and the maximum intensity is a factor of 3 lower than the measured thresholds of the 6.3-ps pulse. The laser contrast before -12 ps shows lower maximum intensities and fluences (details in Appendix B).

The scaling of laser contrast measurements to absolute intensity, however, has to be considered with caution. In principle, the pulse shape in the focal spot where the plasma dynamics are induced could be different from the laser pulse characteristics measured from the nonfocused laser beam, e.g., due to spatiotemporal couplings [70]. In view of this, the presented comparison shows surprisingly good agreement. To summarize, the LIB at $5.7 \times 10^{21} \text{ W/cm}^2$ peak intensity most likely originates from the accumulation of intensity between $I_{\text{th}}^{\text{fit}}[6 \text{ ps}]$ and $I_{\text{th}}^{\text{fit}}[30 \text{ ps}]$ for a duration of between 6 ps and 30 ps prior to about -3 ps delay.

The example demonstrates the methodology of how the onset of LIB can be derived from a laser contrast measurement. The onset of LIB is not triggered by the first intersection with a certain threshold intensity, but by a continuous temporal accumulation of intensity at a certain

level for a specific duration. If the accumulated intensity, i.e., the deposited fluence, reaches the threshold fluence $F_{\text{th}}[\tau]$ of a comparable pulse duration τ within an order of magnitude, the subsequent onset of LIB must be expected.

Furthermore, the comparison between the lowest and the highest peak intensity settings demonstrates the relevance of the pulse duration dependence of LIB to the starting point of LIB in ultrarelativistic laser-solid interactions. As laser peak intensity increases, the intensities in the leading edge also increase. The simplified assumption of a fixed intensity threshold of LIB, for example the classical BSI threshold, would shift the starting point of LIB only slightly to earlier times, depending on the leading edge intensity evolution. However, if the slowly rising picosecond pedestal enters the relevant intensity range of LIB, the starting point of LIB is actually shifted to earlier times by a lowering of the applicable threshold intensity. Figure 2(a) shows that the relevant intensity range varies significantly with pulse duration, i.e., pedestal duration.

Still, an important prerequisite of such an analysis is a temporally well-resolved and quantitatively valid laser contrast measurement. To capture the strong field ionization effects, single femtosecond temporal resolution is desired especially for short prepulses. The picosecond pedestal-induced avalanche ionization imposes the measurement of intensities lower than about 10^{11} W/cm^2 , which is a required dynamic range higher than 10^{11} for current petawatt-class laser systems. Considering the intrinsic leading edge of these laser systems without any temporal contrast cleaning, a time window of at least 100 ps is needed.

Several commercial products based on third-order autocorrelation are available and the development is progressing towards higher dynamic range [22] and operation at single shot [24,71]. However, an exploration of the limitations of existing technology is desired and the design of additional techniques like self-referenced spectral interferometry with extended time excursion (SRSI-ETE) [23,72] is promising to reliably quantify absolute intensity levels in the leading edge that are highly relevant to LIB, target preexpansion, and preheating in high-intensity laser-solid experiments.

V. OUTLOOK

We demonstrated that the onset of LIB in high-intensity petawatt-class laser interactions with dielectric targets is highly sensitive to the leading edge intensity evolution. To avoid complex ionization dynamics that are prone to small changes of the leading edge or variations of the local target properties and to facilitate a well-predictable onset of LIB in similar experiments, the strong field ionization regime appears to be favorable. Experimentally, there are two promising approaches. Commonly, experiments rely on a steep rising edge towards the laser peak, i.e., a reduction

of the pedestal height [40]. We propose a complementary approach, which is the implementation of an artificial femtosecond prepulse with an intensity above a characterized threshold intensity of LIB, e.g., I_{th} [30 fs]. The prepulse is inserted at a known delay before the leading edge enters the relevant intensity levels of LIB, for example at -12 ps in the presented highest peak intensity setting. The prepulse initializes LIB and, by this, increases the electron density in the conduction band above the critical plasma density. This leads to a localized laser energy deposition of the following laser light, e.g., by inverse Bremsstrahlung. In a start-to-end simulation of the high-intensity laser-solid interaction and starting from the artificial prepulse, the target preexpansion by the leading edge can then be directly simulated in a radiation-hydrodynamics framework. Especially for leading edges with tens to hundreds of picosecond duration the procedure will improve the agreement between start-to-end simulations and experiments that aim to optimize target preexpansion, e.g., for enhanced laser-driven ion acceleration [26].

VI. CONCLUSION

In summary, we report on the time-resolved observation of LIB of a dielectric cryogenic hydrogen sheet-jet target during the leading edge of high-contrast petawatt-class laser pulses with peak intensities between 0.6×10^{21} and $5.7 \times 10^{21} \text{ W/cm}^2$. By switching from the lowest to the highest peak intensity, a shift of the onset of LIB from the foot of the steep rising edge into the picosecond pedestal of the leading edge occurs. The temporal shift is attributed to an increased absolute intensity level in the picosecond pedestal, which lowers the applicable threshold intensity of LIB well below the appearance intensity I_{app} of the barrier suppression ionization model. The observation clearly demonstrates that the laser pulse duration dependence of LIB and LIDT affect the onset of LIB in high-intensity laser-solid experiments.

To generalize the observation to other laser-target systems, we present an approach to infer the starting point of LIB from laser contrast measurements compared to a characterization study of target-specific thresholds of LIB.

The pulse duration dependence of LIB and its coupling to the leading edge intensity evolution requires careful consideration of target-specific breakdown thresholds to determine the correct starting point for modeling target preexpansion in start-to-end simulations of high-intensity laser-solid interactions.

ACKNOWLEDGMENTS

C.B. thanks P. Balling for fruitful correspondence and M. Kuntzsch, M. Loeser, and M. Siebold for the excellent support in the operation of the probe laser system. The work is partially supported by H2020 Laserlab Europe V (PRISES, Contract No. 871124). The work of C.B.C,

M.G., S.H.G., C.S., and F.T. is supported by the U.S. DOE Office of Science, Fusion Energy Sciences under FWP No. 100182. C.B.C. acknowledges partial support from the Natural Sciences and Engineering Research Council of Canada (NSERC). F.T. is supported by the National Nuclear Security Administration (NNSA) and by the German Academic Scholarship Foundation. C.B., F.-E.B., C.B.C., L.G., M.G., S.G., S.K., F.K., L.O.-H., M.R., H.-P.S., C.S., F.T., T.Z., K.Z. conducted the experiments at ultrarelativistic laser intensity. C.B. analyzed the corresponding experimental shadowgraphy data. S.B., R.G., U.H., T.P. conducted the laser contrast measurement and operated the DRACO PW laser. S.A., C.B., M.R., M.V., K.Z. conducted the characterization study about the pulse duration dependence of LIB. S.A., C.B. analyzed the characterization study. S.A., C.B., M.G., T.K., M.R., K.Z. discussed the ionization mechanisms leading to LIB. C.B. prepared the figures and wrote the manuscript. T.E.C., S.H.G., U.S., and K.Z. supervised the project. All authors reviewed the manuscript. The authors declare no competing interests.

APPENDIX A: PULSE DURATION DEPENDENCE OF LIB—METHODOLOGY

The goal of the characterization study is the measurement of the threshold fluences F_{th} and threshold intensities I_{th} of LIB of the cryogenic hydrogen sheet-jet target for different laser pulse durations. For this purpose, the pump laser energy is attenuated by about 6 orders of magnitude. The attenuation is achieved by multiple wedges and a reduction of the beam diameter by a circular aperture in front of the OAP. This generates an Airy pattern focus on target with $14 \mu\text{m}$ FWHM of the central disk. The residual pump laser energy can be scanned between 10% and 100% via the rotation of a wave plate and pairs of thin-film polarizers in the beam path before compression. The temporal pulse characteristics of the pump laser are preserved during attenuation. Six different settings of pulse duration are realized by introducing a defined chirp via an acousto-optic programmable dispersive filter (settings 1, 2, 3, 4) and an SF6 glass block (settings 5, 6) in the stretched beam path of the laser system. For all settings, the temporal pulse shape [Figs. 5(b) and 5(c)] and the peak intensity are inferred from the measured laser spectrum [Fig. 5(a)], the artificially introduced spectral phase, the laser energy, and a measurement of the focal spot. The peak fluence is calculated using the laser energy and the measurement of the focal spot only. For setting 1 (zero spectral phase), the pulse duration is verified by measurements with a *Wizzler* device by Fastlite. The different settings are summarized in Table II.

For each pulse duration setting, the threshold intensity I_{th} and threshold fluence F_{th} are derived as follows. The repetition rate of the pump laser and the self-replenishing

TABLE II. Measured threshold fluence F_{th} and threshold intensity I_{th} of LIB of the hydrogen sheet-jet target for the different settings of group delay dispersion (GDD) and third-order dispersion (TOD). The FWHM of the laser pulse duration τ is derived from the calculated pulse envelopes [Figs. 5(b) and 5(c)].

Setting	GDD (fs ²)	TOD (fs ³)	τ (ps)	F_{th} (J/cm ²)	I_{th} (W/cm ²)
1	0	0	0.0285	3.4 ± 0.4	$(1.1 \pm 0.2) \times 10^{14}$
2	500	0	0.0445	4.1 ± 0.7	$(7.2 \pm 1.2) \times 10^{13}$
3	2000	0	0.296	5.4 ± 0.7	$(1.8 \pm 0.3) \times 10^{13}$
4	6000	0	0.954	8.3 ± 0.7	$(9.3 \pm 0.8) \times 10^{12}$
5	19 536	12 320	3.17	8.6 ± 1.9	$(2.9 \pm 0.6) \times 10^{12}$
6	38 612	24 290	6.33	14 ± 2	$(2.4 \pm 0.4) \times 10^{12}$

target delivery of the cryogenic hydrogen jet allow us to generate laser-target interactions at 1 Hz. Each interaction is visualized via time-resolved optical shadowgraphy probing with a similar setup as presented in Sec. II A and Fig. 1. The probe delay is fixed to 1 ps after the falling flank of the pump pulse. Time delay scans for different pulse duration settings show that the influence of recombination

is negligible at this delay. To find the threshold of LIB, a laser energy scan is conducted for each setting. The transmission of the wave-plate attenuator is reduced stepwise from 100% down to 10%. The pulse energy before the transmission attenuator is adjusted such that, for the 100% setting, LIB is assured and it can be ruled out for the 10% setting. Thousands of shots at 10 to 14 transmission attenuator settings are acquired for each pulse duration setting. A secondary optical probing axis allows us to sort the data by target rotation angle and to use hundreds of shots for a statistical evaluation of the laser energy scan. Assuming an underlying normal distribution of fluctuations in laser and target properties, the distribution function of the fraction of shots with LIB as a function of laser energy is an error function. The threshold of LIB is given by the laser energy at which the error function reaches 50%. The standard deviation of the threshold value is given by the width of the error function. The resulting values for I_{th} and F_{th} are given in Table II.

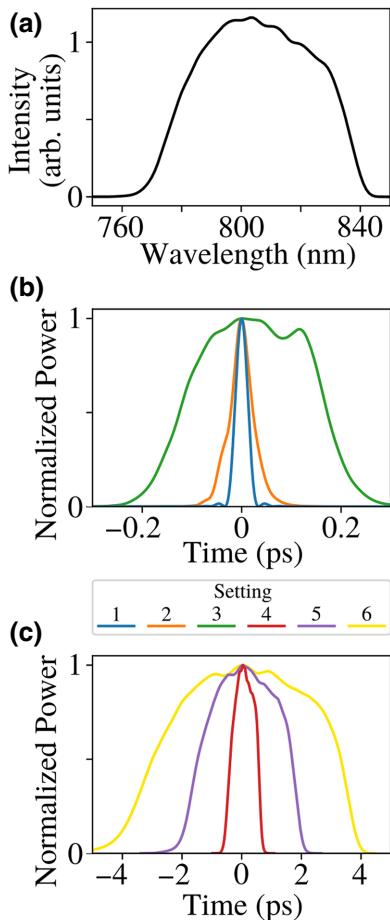


FIG. 5. Pump laser properties for the measurement of the pulse duration dependence of LIB. (a) Spectrum, (b) temporal pulse envelope of settings 1, 2, 3, and (c) temporal pulse envelope of settings 4, 5, 6 (refer to Table II).

APPENDIX B: LASER CONTRAST

The laser contrast measurement of the leading edge is performed with a scanning third-order autocorrelator (TOAC; *Sequoia HD* device by Amplitude). The TOAC has a dynamic range $>10^{13}$, a temporal scan resolution <16 fs, and an optical temporal resolution <100 fs. The pump laser operation at reduced pulse energy (0.27 J before compression) allows for the acquisition of thousands of shots and thus a high sampling rate of the leading edge without degradation of the compressor gratings. The final amplification stage of the laser amplifiers is known to induce time-dependent changes of the leading edge and to manipulate the height of individual short prepulses [73–75]. A measurement of the laser contrast at highest laser energy (32 J before compression) and a measurement at 4.2 J before compression are conducted via a pick-off mirror in the collimated beam path before final focusing during a different experimental campaign. They allow us to calculate a laser system-specific conversion function, which enables the computation of the laser contrast at highest laser energy from a TOAC measurement at reduced laser

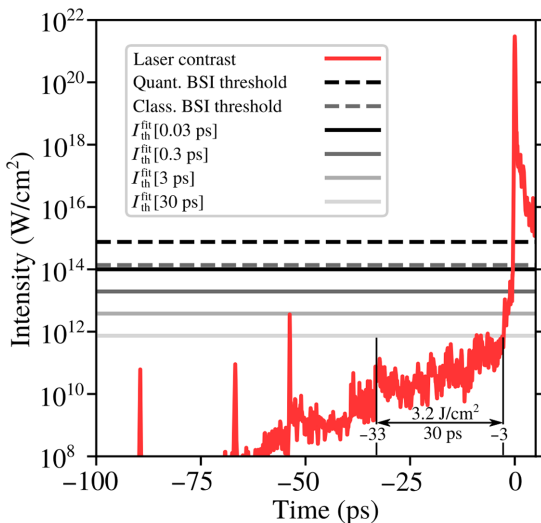


FIG. 6. Leading edge of the pump laser (laser contrast) in the highest peak intensity setting (red line). The quantum mechanical and classical BSI thresholds are given together with the fitted intensity thresholds of LIB $I_{\text{th}}^{\text{fit}}[\tau]$ for four different pulse durations τ (horizontal lines).

energy, frequently measured for all experimental campaigns. The hereby calculated laser contrast resembles the intrinsic laser contrast of the pump laser system at full amplification with a high sampling rate and for a specific experimental campaign.

For the plasma mirror device, a contrast enhancement factor of 2×10^{-4} is derived by two independent methods [(1) scanning TOAC at highest laser energy with and without a plasma mirror, (2) a spectrally and angularly resolved reflectance measurement of the plasma mirror substrate]. Measurements of the intrinsic and the plasma-mirror-enhanced laser contrasts via SRSI-ETE [23,72] put the timing of the plasma mirror switching point between -0.3 and -0.2 ps before the laser peak. Using these results, the intrinsic laser contrast at full amplification is converted to the plasma-mirror-enhanced laser contrast at full amplification. Taking the mean target rotation angle into account, the calculated laser contrast is scaled to the respective peak intensity of each setting and displayed in Figs. 4 and 6.

The laser contrast of the highest peak intensity setting in Fig. 6 shows a prepulse with $3.6 \times 10^{12} \text{ W/cm}^2$ peak intensity at -54 ps. The pulse duration of the prepulse is limited by the optical temporal resolution of the TOAC measurement to $\tau < 100$ fs. The intensity threshold of LIB of a 100-fs pulse is $I_{\text{th}}^{\text{fit}}[100 \text{ fs}] = 4.3 \times 10^{13} \text{ W/cm}^2$ and shorter pulses feature an even higher threshold intensity. Even assuming an uncertainty of one order of magnitude for the intensity level of the laser contrast, the prepulse is insufficient to initiate LIB, in agreement with the time-resolved optical shadowgraphy measurements.

Temporal integration of the laser contrast between -33 and -3 ps yields a fluence of 3.2 J/cm^2 (Fig. 6). This is about a factor of 6 lower than the fitted damage fluence $F_{\text{th}}^{\text{fit}}[30 \text{ ps}] = 18.1 \text{ J/cm}^2$, similar to the case of the plateau between -10 and -3 ps that is discussed in Sec. IV. However, this implies that the picosecond pedestal between -33 and -12 ps contains only 1 J/cm^2 , which is more than a factor of 16 below the fluence threshold $F_{\text{th}}^{\text{fit}}[21 \text{ ps}] = 16.6 \text{ J/cm}^2$. The observation of LIB in the highest peak intensity setting is thus most likely caused by the plateau of the picosecond pedestal between -10 and -3 ps.

- [1] M. Roth, Review on the current status and prospects of fast ignition in fusion targets driven by intense, laser generated proton beams, *Plasma Phys. Controlled Fusion* **51**, 014004 (2008).
- [2] J. Fernández, B. Albright, F. Beg, F. Foord, B. Hegelich, J. Honrubia, M. Roth, R. Stephens, and L. Yin, Fast ignition with laser-driven proton and ion beams, *Nucl. Fusion* **54**, 054006 (2014).
- [3] F. Albert, *et al.*, 2020 roadmap on plasma accelerators, *New J. Phys.* **23**, 031101 (2021).
- [4] S. Chen, S. Atzeni, M. Gauthier, D. Higginson, F. Mangia, J.-R. Marques, R. Riquier, and J. Fuchs, Proton stopping power measurements using high intensity short pulse lasers produced proton beams, *Nucl. Instrum. Methods Phys. Res. Section A* **740**, 105 (2014).
- [5] J. Ren, *et al.*, Observation of a high degree of stopping for laser-accelerated intense proton beams in dense ionized matter, *Nat. Commun.* **11**, 5157 (2020).
- [6] A. S. Martynenko, S. A. Pikuz, L. Antonelli, F. Barbato, G. Boutoux, L. Giuffrida, J. J. Honrubia, E. Hume, J. Jacoby, D. Khaghani, K. Lancaster, P. Neumayer, O. N. Rosmej, J. J. Santos, O. Turianska, and D. Batani, Role of relativistic laser intensity on isochoric heating of metal wire targets, *Opt. Express* **29**, 12240 (2021).
- [7] L. B. Fletcher, *et al.*, Electron-ion temperature relaxation in warm dense hydrogen observed with picosecond resolved X-ray scattering, *Front. Phys.* **10**, 2296 (2022).
- [8] M. Borghesi, D. H. Campbell, A. Schiavi, M. G. Haines, O. Willi, A. J. MacKinnon, P. Patel, L. A. Gizzi, M. Galimberti, R. J. Clarke, F. Pegoraro, H. Ruhl, and S. Bulanov, Electric field detection in laser-plasma interaction experiments via the proton imaging technique, *Phys. Plasmas* **9**, 2214 (2002).
- [9] L. Romagnani, J. Fuchs, M. Borghesi, P. Antici, P. Audibert, F. Ceccherini, T. Cowan, T. Grismayer, S. Kar, A. Macchi, P. Mora, G. Pretzler, A. Schiavi, T. Toncian, and O. Willi, Dynamics of Electric Fields Driving the Laser Acceleration of Multi-MeV Protons, *Phys. Rev. Lett.* **95**, 195001 (2005).
- [10] P. Chaudhary, G. Milluzzo, H. Ahmed, B. Odlozilik, A. McMurray, K. M. Prise, and M. Borghesi, Radiobiology experiments with ultra-high dose rate laser-driven protons: Methodology and state-of-the-art, *Front. Phys. (Lausanne)* **9**, 75 (2021).

- [11] F. Kroll, *et al.*, Tumour irradiation in mice with a laser-accelerated proton beam, *Nat. Phys.* **18**, 316 (2022).
- [12] H. Daido, M. Nishiuchi, and A. S. Pirozhkov, Review of laser-driven ion sources and their applications, *Rep. Prog. Phys.* **75**, 056401 (2012).
- [13] A. Macchi, M. Borghesi, and M. Passoni, Ion acceleration by superintense laser-plasma interaction, *Rev. Mod. Phys.* **85**, 751 (2013).
- [14] J. Schreiber, P. Bolton, and K. Parodi, Invited review article: “Hands-on” laser-driven ion acceleration: A primer for laser-driven source development and potential applications, *Rev. Sci. Instrum.* **87**, 071101 (2016).
- [15] C. N. Danson, *et al.*, Petawatt and exawatt class lasers worldwide, *High Power Laser Sci. Eng.* **7**, e54 (2019).
- [16] X. Lu, H. Zhang, J. Li, and Y. Leng, Reducing temporal pedestal in a Ti:sapphire chirped-pulse amplification system by using a stretcher based on two concave mirrors, *Opt. Lett.* **46**, 5320 (2021).
- [17] D. Hillier, C. Danson, S. Duffield, D. Egan, S. Elsmere, M. Girling, E. Harvey, N. Hopps, M. Norman, S. Parker, P. Treadwell, D. Winter, and T. Bett, Ultrahigh contrast from a frequency-doubled chirped-pulse-amplification beamline, *Appl. Opt.* **52**, 4258 (2013).
- [18] C. Thaury, F. Quéré, J.-P. Geindre, A. Levy, T. Ceccotti, P. Monot, M. Bougeard, F. Réau, P. d’Oliveira, P. Audebert, R. Marjoribanks, and P. Martin, Plasma mirrors for ultrahigh-intensity optics, *Nat. Phys.* **3**, 424 (2007).
- [19] L. Obst, J. Metzkes-Ng, S. Bock, G. E. Cochran, T. E. Cowan, T. Oksenhendler, P. L. Poole, I. Prencipe, M. Rehwald, C. Rödel, H.-P. Schlenvoigt, U. Schramm, D. W. Schumacher, T. Ziegler, and K. Zeil, On-shot characterization of single plasma mirror temporal contrast improvement, *Plasma Phys. Controlled Fusion* **60**, 054007 (2018).
- [20] G. Priebe, K. Janulewicz, V. Redkorechey, J. Tümmeler, and P. Nickles, Pulse shape measurement by a non-collinear third-order correlation technique, *Opt. Commun.* **259**, 848 (2006).
- [21] V. N. Ginzburg, N. V. Didenko, A. V. Konyashchenko, V. V. Lozhkarev, G. A. Luchinin, A. P. Lutsenko, S. Y. Mironov, E. A. Khazanov, and I. V. Yakovlev, Third-order correlator for measuring the time profile of petawatt laser pulses, *Quantum Electron.* **38**, 1027 (2008).
- [22] V. A. Schanz, F. Wagner, M. Roth, and V. Bagnoud, Noise reduction in third order cross-correlation by angle optimization of the interacting beams, *Opt. Express* **25**, 9252 (2017).
- [23] T. Oksenhendler, P. Bizouard, O. Albert, S. Bock, and U. Schramm, High dynamic, high resolution and wide range single shot temporal pulse contrast measurement, *Opt. Express* **25**, 12588 (2017).
- [24] J. Ma, P. Yuan, J. Wang, G. Xie, H. Zhu, and L. Qian, Single-shot cross-correlator for pulse-contrast characterization of high peak-power lasers, *High Power Laser Sci. Eng.* **6**, e61 (2018).
- [25] K. Matsukado, *et al.*, Energetic Protons from a Few-Micron Metallic Foil Evaporated by an Intense Laser Pulse, *Phys. Rev. Lett.* **91**, 215001 (2003).
- [26] M. Nishiuchi, *et al.*, Dynamics of laser-driven heavy-ion acceleration clarified by ion charge states, *Phys. Rev. Res.* **2**, 033081 (2020).
- [27] N. P. Dover, M. Nishiuchi, H. Sakaki, K. Kondo, M. A. Alkhimova, A. Y. Faenov, M. Hata, N. Iwata, H. Kiriyama, J. K. Koga, T. Miyahara, T. A. Pikuz, A. S. Pirozhkov, A. Sagisaka, Y. Sentoku, Y. Watanabe, M. Kando, and K. Kondo, Effect of Small Focus on Electron Heating and Proton Acceleration in Ultrarelativistic Laser-Solid Interactions, *Phys. Rev. Lett.* **124**, 084802 (2020).
- [28] M. Schollmeier, A. B. Sefkow, M. Geissel, A. V. Arefiev, K. A. Flippo, S. A. Gaillard, R. P. Johnson, M. W. Kimmel, D. T. Offermann, P. K. Rambo, J. Schwarz, and T. Shimada, Laser-to-hot-electron conversion limitations in relativistic laser matter interactions due to multi-picosecond dynamics, *Phys. Plasmas* **22**, 043116 (2015).
- [29] F. Wagner, O. Depert, C. Brabetz, P. Fiala, A. Kleinschmidt, P. Poth, V. A. Schanz, A. Tebartz, B. Zielbauer, M. Roth, T. Stöhlker, and V. Bagnoud, Maximum Proton Energy above 85 MeV from the Relativistic Interaction of Laser Pulses with Micrometer Thick CH₂ Targets, *Phys. Rev. Lett.* **116**, 205002 (2016).
- [30] I. J. Kim, K. H. Pae, I. W. Choi, C.-L. Lee, H. T. Kim, H. Singhal, J. H. Sung, S. K. Lee, H. W. Lee, P. V. Nickles, T. M. Jeong, C. M. Kim, and C. H. Nam, Radiation pressure acceleration of protons to 93 MeV with circularly polarized petawatt laser pulses, *Phys. Plasmas* **23**, 070701 (2016).
- [31] A. Higginson, R. J. Gray, M. King, R. J. Dance, S. D. R. Williamson, N. M. H. Butler, R. Wilson, R. Capdessus, C. Armstrong, J. S. Green, S. J. Hawkes, P. Martin, W. Q. Wei, S. R. Mirfayzi, X. H. Yuan, S. Kar, M. Borghesi, R. J. Clarke, D. Neely, and P. McKenna, Near-100 MeV protons via a laser-driven transparency-enhanced hybrid acceleration scheme, *Nat. Commun.* **9**, 1 (2018).
- [32] T. Ziegler *et al.* Proton beam quality enhancement by spectral phase control of a PW-class laser system, *Sci. Rep.* **11**, 7338 (2021).
- [33] K. Zeil, J. Metzkes, T. Kluge, M. Bussmann, T. E. Cowan, S. D. Kraft, R. Sauerbrey, and U. Schramm, Direct observation of prompt pre-thermal laser ion sheath acceleration, *Nat. Commun.* **3**, 1 (2012).
- [34] S. Augst, D. Strickland, D. D. Meyerhofer, S. L. Chin, and J. H. Eberly, Tunneling Ionization of Noble Gases in a High-Intensity Laser Field, *Phys. Rev. Lett.* **63**, 2212 (1989).
- [35] NIST atomic spectra database ionization energies, <https://physics.nist.gov/PhysRefData/ASD/ionEnergy.html> (accessed 13-July-2022).
- [36] D. Bauer and P. Mulser, Exact field ionization rates in the barrier-suppression regime from numerical time-dependent Schrödinger-equation calculations, *Phys. Rev. A* **59**, 569 (1999).
- [37] B. Rethfeld, D. S. Ivanov, M. E. Garcia, and S. I. Anisimov, Modelling ultrafast laser ablation, *J. Phys. D: Appl. Phys.* **50**, 193001 (2017).
- [38] M. Lenzner and W. Rudolph, *Laser-Induced Optical Breakdown in Solids* (Springer, New York, NY, 2008), p. 243.
- [39] P. Balling and J. Schou, Femtosecond-laser ablation dynamics of dielectrics: Basics and applications for thin films, *Rep. Prog. Phys.* **76**, 036502 (2013).
- [40] D. Wang, Y. Shou, P. Wang, J. Liu, Z. Mei, Z. Cao, J. Zhang, P. Yang, G. Feng, S. Chen, Y. Zhao, J. Schreiber, and W. Ma, Laser-induced damage thresholds of ultrathin

- targets and their constraint on laser contrast in laser-driven ion acceleration experiments, *High Power Laser Sci. Eng.* **8**, e41 (2020).
- [41] R. Stoian, M. Boyle, A. Thoss, A. Rosenfeld, G. Korn, I. V. Hertel, and E. E. B. Campbell, Laser ablation of dielectrics with temporally shaped femtosecond pulses, *Appl. Phys. Lett.* **80**, 353 (2002).
- [42] E. Louzon, Z. Henis, S. Pecker, Y. Ehrlich, D. Fisher, M. Fraenkel, and A. Zigler, Reduction of damage threshold in dielectric materials induced by negatively chirped laser pulses, *Appl. Phys. Lett.* **87**, 241903 (2005).
- [43] L. Englert, M. Wollenhaupt, L. Haag, C. Sarpe-Tudoran, B. Rethfeld, and T. Baumert, Material processing of dielectrics with temporally asymmetric shaped femtosecond laser pulses on the nanometer scale, *Appl. Phys. A* **92**, 749 (2008).
- [44] A. Ollé, J. Luce, N. Roquin, C. Rouyer, M. Sozet, L. Gallais, and L. Lamaignère, Implications of laser beam metrology on laser damage temporal scaling law for dielectric materials in the picosecond regime, *Rev. Sci. Instrum.* **90**, 073001 (2019).
- [45] V. S. Popov, Tunnel and multiphoton ionization of atoms and ions in a strong laser field (Keldysh theory), *Phys.-Uspekhi* **47**, 855 (2004).
- [46] S. Popruzhenko, Keldysh theory of strong field ionization: History, applications, difficulties and perspectives, *J. Phys. B* **47**, 204001 (2014).
- [47] B. Chimier, O. Utéza, N. Sanner, M. Sentis, T. Itina, P. Lassonde, F. Légaré, F. Vidal, and J. C. Kieffer, Damage and ablation thresholds of fused-silica in femtosecond regime, *Phys. Rev. B* **84**, 094104 (2011).
- [48] J.-L. Déziel, L. J. Dubé, and C. Varin, Dynamical rate equation model for femtosecond laser-induced breakdown in dielectrics, *Phys. Rev. B* **104**, 045201 (2021).
- [49] B. C. Stuart, M. D. Feit, S. Herman, A. M. Rubenchik, B. W. Shore, and M. D. Perry, Nanosecond-to-femtosecond laser-induced breakdown in dielectrics, *Phys. Rev. B* **53**, 1749 (1996).
- [50] G. Petrov and J. Davis, Interaction of intense ultra-short laser pulses with dielectrics, *J. Phys. B: At., Mol. Opt. Phys.* **41**, 025601 (2008).
- [51] B. H. Christensen and P. Balling, Modeling ultrashort-pulse laser ablation of dielectric materials, *Phys. Rev. B* **79**, 155424 (2009).
- [52] D. Papadopoulos, J. Zou, C. L. Blanc, G. Chériaux, P. Georges, F. Druon, G. Mennerat, P. Ramirez, L. Martin, A. Fréneaux, A. Beluze, N. Lebas, P. Monot, F. Mathieu, and P. Audebert, The Apollon 10 PW laser: Experimental and theoretical investigation of the temporal characteristics, *High Power Laser Sci. Eng.* **4**, e34 (2016).
- [53] J. H. Sung, H. W. Lee, J. Y. Yoo, J. W. Yoon, C. W. Lee, J. M. Yang, Y. J. Son, Y. H. Jang, S. K. Lee, and C. H. Nam, 4.2 PW, 20 fs Ti:sapphire laser at 0.1 Hz, *Opt. Lett.* **42**, 2058 (2017).
- [54] H. Kiriyama, A. S. Pirozhkov, M. Nishiuchi, Y. Fukuda, K. Ogura, A. Sagisaka, Y. Miyasaka, M. Mori, H. Sakaki, N. P. Dover, K. Kondo, J. K. Koga, T. Z. Esirkepov, M. Kando, and K. Kondo, High-contrast high-intensity repetitive petawatt laser, *Opt. Lett.* **43**, 2595 (2018).
- [55] Z. Zhang, F. Wu, J. Hu, X. Yang, J. Gui, P. Ji, X. Liu, C. Wang, Y. Liu, X. Lu, Y. Xu, Y. Leng, R. Li, and Z. Xu, The 1 PW/0.1 Hz laser beamline in SULF facility, *High Power Laser Sci. Eng.* **8**, e4 (2020).
- [56] L. Jiang and H. Tsai, Energy transport and material removal in wide bandgap materials by a femtosecond laser pulse, *Int. J. Heat Mass Transf.* **48**, 487 (2005).
- [57] J. B. Kim, S. Göde, and S. H. Glenzer, Development of a cryogenic hydrogen microjet for high-intensity, high-repetition rate experiments, *Rev. Sci. Instrum.* **87**, 11E328 (2016).
- [58] C. B. Curry, C. Schoenwaelder, S. Goede, J. B. Kim, M. Rehwald, F. Treffert, K. Zeil, S. H. Glenzer, and M. Gauthier, Cryogenic liquid jets for high repetition rate discovery science, *J. Visualized Exp. JoVE*, e61130 (2020).
- [59] S. Göde, C. Rödel, K. Zeil, R. Mishra, M. Gauthier, F.-E. Brack, T. Kluge, M. J. MacDonald, J. Metzkes, L. Obst, M. Rehwald, C. Ruyer, H.-P. Schlenvoigt, W. Schumaker, P. Sommer, T. E. Cowan, U. Schramm, S. Glenzer, and F. Fiuzza, Relativistic Electron Streaming Instabilities Modulate Proton Beams Accelerated in Laser-Plasma Interactions, *Phys. Rev. Lett.* **118**, 194801 (2017).
- [60] L. Obst, *et al.*, Efficient laser-driven proton acceleration from cylindrical and planar cryogenic hydrogen jets, *Sci. Rep.* **7**, 10248 (2017).
- [61] T. Ziegler, *et al.*, Optical probing of high intensity laser interaction with micron-sized cryogenic hydrogen jets, *Plasma Phys. Controlled Fusion* **60**, 074003 (2018).
- [62] J. Polz, A. P. L. Robinson, A. Kalinin, G. A. Becker, R. A. C. Fraga, M. Hellwing, M. Hornung, S. Keppler, A. Kessler, D. Klöpfel, H. Liebetrau, F. Schorcht, J. Hein, M. Zepf, R. E. Grisenti, and M. C. Kaluza, Efficient laser-driven proton acceleration from a cryogenic solid hydrogen target, *Sci. Rep.* **9**, 16534 (2019).
- [63] C. Bernert, *et al.*, Off-harmonic optical probing of high intensity laser plasma expansion dynamics in solid density hydrogen jets, *Sci. Rep.* **12**, 7287 (2022).
- [64] U. Schramm, *et al.*, First results with the novel petawatt laser acceleration facility in Dresden, *J. Phys. Conf. Ser.* **874**, 012028 (2017).
- [65] M. Kühnel, J. M. Fernández, G. Tejeda, A. Kalinin, S. Montero, and R. E. Grisenti, Time-Resolved Study of Crystallization in Deeply Cooled Liquid Parahydrogen, *Phys. Rev. Lett.* **106**, 245301 (2011).
- [66] K. Inoue, H. Kanzaki, and S. Suga, Fundamental absorption spectra of solid hydrogen, *Solid State Commun.* **30**, 627 (1979).
- [67] D. Haffa, J. Bin, M. Speicher, K. Allinger, J. Hartmann, C. Kreuzer, E. Ridente, T. M. Ostermayr, and J. Schreiber, Temporally resolved intensity contouring (TRIC) for characterization of the absolute spatio-temporal intensity distribution of a relativistic, femtosecond laser pulse, *Sci. Rep.* **9**, 7697 (2019).
- [68] T. Kluge, T. Cowan, A. Debus, U. Schramm, K. Zeil, and M. Bussmann, Electron Temperature Scaling in Laser Interaction with Solids, *Phys. Rev. Lett.* **107**, 205003 (2011).
- [69] G. K. Ngirmang, J. T. Morrison, K. M. George, J. R. Smith, K. D. Frische, C. Orban, E. A. Chowdhury, and W. M. Roquemore, Evidence of radial Weibel instability

- in relativistic intensity laser-plasma interactions inside a sub-micron thick liquid target, *Sci. Rep.* **10**, 9872 (2020).
- [70] A. Jeandet, *et al.*, Survey of spatio-temporal couplings throughout high-power ultrashort lasers, *Opt. Express* **30**, 3262 (2022).
- [71] J. Ma, P. Yuan, X. Ouyang, J. Wang, G. Xie, and L. Qian, Demonstration of single-shot measurements of 10^{13} ultrahigh-contrast pulses by manipulating cross-correlation, *Adv. Photonics Res.* **2**, 2100105 (2021).
- [72] T. Oksenhendler, Self-referenced spectral interferometry theory, Preprint [ArXiv:1204.4949](https://arxiv.org/abs/1204.4949) (2012).
- [73] H. Kiriyama, Y. Miyasaka, A. Sagisaka, K. Ogura, M. Nishiuchi, A. S. Pirozhkov, Y. Fukuda, M. Kando, and K. Kondo, Experimental investigation on the temporal contrast of pre-pulses by post-pulses in a petawatt laser facility, *Opt. Lett.* **45**, 1100 (2020).
- [74] A. Kon, M. Nishiuchi, H. Kiriyama, M. Kando, S. Bock, T. Ziegler, T. Pueschel, K. Zeil, U. Schramm, and K. Kondo, Single-shot measurement of post-pulse-generated pre-pulse in high-power laser systems, *Crystals* **10**, 657 (2020).
- [75] S. Bock, F. M. Herrmann, T. Püschel, U. Helbig, R. Gebhardt, J. J. Lötfering, R. Pausch, K. Zeil, T. Ziegler, A. Irman, T. Oksenhendler, A. Kon, M. Nishiuchi, H. Kiriyama, K. Kondo, T. Toncian, and U. Schramm, Characterization of accumulated B -integral of regenerative amplifier based CPA systems, *Crystals* **10**, 847 (2020).